The size distributions of nanoscale Fe-Ni-S droplets in Stardust melted grains from comet 81P/Wild 2

Nathan E. SANDERS[1,2] and Michael A. VELBEL[3*]

[1]Department of Physics and Astronomy, Michigan State University, East Lansing, MI 48824, USA
[2]Department of Astronomy, Harvard University, Cambridge, MA 02138, USA
[3]Department of Geological Sciences, 206 Natural Science Building, Michigan State University, East Lansing, MI 48824–1115, USA
[*]Corresponding author. E-mail: velbel@msu.edu

Abstract–To constrain the effects of capture modification processes, the size distribution of nanoscale refractory Fe-Ni-S inclusions ("droplets") was measured in five allocations extracted from throughout the depth of Stardust Track 35. The Fe∕S ratio has been previously shown to increase significantly with penetration depth in this track, suggesting increasing capture-related modification along the track. Astronomical image analysis tools were employed to measure the sizes of more than 8000 droplets from TEM images, and completeness simulations were used to correct the distribution for detection bias as a function of radius. The size distribution characteristics are found to be similar within independent regions of individual allocations, demonstrating uniformity within grains. The size distribution of the Fe-Ni-S droplets in each allocation is dominated by a mode near 11 nm, but is coarse-skewed and leptokurtic with a mean of ∼17 nm and a standard deviation of ∼9 nm. The size distribution characteristics do not vary systematically with penetration depth, despite the strong trend in bulk Fe∕S ratio. This suggests that the capture modification process is not primarily responsible for producing the morphology of these nanoscale droplets. The Stardust Track 35 droplet size distribution indicates slightly smaller sizes, but otherwise resembles those in carbonaceous chondrite Acfer 094, and chondritic porous interplanetary dust particles that escaped nebular annealing of sulfides. The size distribution of metal-sulfide beads in Stardust's quenched melted-grain emulsions appears to be inherited from the size distribution of unmelted sulfide mineral grains in comet-dust particles of chondritic character.

INTRODUCTION

Overview

In January 2004, the NASA Stardust spacecraft encountered the coma of comet 81P/Wild 2 at a relative velocity of 6.1 km s^{-1}. Cometary particles were captured in the spacecraft's gradient density silica aerogel collectors, and the Stardust mission successfully returned the samples to Earth in January 2006 (Brownlee et al. 2003, 2006). Individual microscale cometary dust fragments produced impact tracks of varying morphology in the collector (Hörz et al. 2006; Burchell

et al. 2008; Ebel et al. 2009). The incident particles decelerated over ∼0.3 μs and, because aerogel is highly insulating, kinetic energy conversion during impact caused intense heat pulses lasting approximately a microsecond, peak temperatures in excess of 2000 K, thermal gradients of ∼2500 K∕μm near grain surfaces, and sub-millisecond cooling times (Noguchi et al. 2007; Roskosz et al. 2008; Trigo-Rodríguez et al. 2008; Dominguez 2009).

Preliminary examination (PE) of material returned from comet 81P/Wild 2 revealed that approximately half of the first-characterized largest captured grains along and at the termini of the capture tracks show only

limited signs of alteration and consist of olivine, pyroxene, Fe-Ni sulfide, and other minerals largely unmodified by hypervelocity capture in a silica aerogel capture medium (Zolensky et al. 2006). Subsequent research has established multiple similarities between such Stardust "microrocks" (Velbel and Harvey 2009; after Burnett 2006; a.k.a. "nanorocks") and primitive solar-system materials such as chondritic porous (CP) interplanetary dust particles (IDPs) and a number of anhydrous components of chondritic meteorites (Hörz et al. 2006; Zolensky et al. 2006, 2008; Leroux et al. 2008; Nakamura et al. 2008; Tomeoka et al. 2008; Jacob et al. 2009; Joswiak et al. 2009).

Melted grains, which constituted the other half of the grains characterized during PE, are a vesicular amorphous mixture of quench products of melted cometary silicates mixed with molten aerogel, and include an emulsion of spherical nanoscale Fe-Ni-S droplets (Flynn et al. 2006; Hörz et al. 2006; Zolensky et al. 2006; Ishii et al. 2008; Leroux et al. 2008, 2009; Nakamura et al. 2008; Rietmeijer et al. 2008; Roskosz et al. 2008; Tomeoka et al. 2008; Burchell et al. 2009; Fries et al. 2009; Rietmeijer 2009; Stodolna et al. 2009; Velbel and Harvey 2009). Stardust melted grains quenched from an ensemble of multiple immiscible fluids, including Fe-Ni metal melt, Fe($\pm$Ni)-S melt, Mg-rich silicate melt (dominantly melted Mg-silicates), Si-rich melt (dominantly melted silica aerogel), and a vapor phase that produced the vesicles (Leroux et al. 2008; Roskosz et al. 2008; Velbel and Harvey 2009; Rietmeijer 2009).

On the basis of research to date (references in previous paragraphs), it is generally accepted that incident particles consisted of two categories of material that responded differently to aerogel capture, one yielding the observed material that largely survived aerogel capture as "microrocks," and the other yielding the extensively or completely melted grains. However, the specific properties of the category that yielded the melted grains and how those fragments differed (e.g., finer grain size, fluffier incident-particle structure, composition including volatile elements) from the population that survived as "microrocks" remain to be firmly established.

We note that the nomenclature and allocation numbering system used in this article will follow that described by Velbel and Harvey (2009). "Particle" is used to refer to pre-capture projectiles, while "grain" is reserved for captured, extracted solids. Ultramicrotome sections of grains prepared by the Stardust curatorial facility are called "allocations," with identifiers designated by the Stardust Cometary Sample Catalog (Bastien et al. 2006). The terms "bead" and "droplet" are used specifically to indicate nanometer-sized Fe-Ni-S

inclusions identified within allocations and inferred to be solidified from formerly molten liquid.

Modification of Incident Particles During Aerogel Capture

The characterization of aerogel capture modification processes has emerged as an area of research supporting interpretation of Stardust sample analyses (e.g., Bradley et al. 2009). Laboratory experiments using analog materials to simulate Stardust incident particles have indicated several models of track formation (recent examples include Burchell et al. 2008; Trigo-Rodríguez et al. 2008; Burchell et al. 2009; Dominguez 2009; Fries et al. 2009; Kearsley et al. 2009; Tsuchiyama et al. 2009; Wozniakiewicz et al. 2009; Ida et al. 2010; also see citations to earlier papers in Velbel and Harvey 2009). These studies supplement a large body of existing literature on hypervelocity impact experiments, performed in preparation for the Stardust mission and for other applications (for example, Anderson and Ahrens 1994; Burchell et al. 2006, and references therein). Moreover, detailed studies of individual Stardust particles and tracks have been performed using a wide array of analytical techniques (for example, Zolensky et al. 2006; Ebel et al. 2009; Jacob et al. 2009; Stodolna et al. 2009; Velbel and Harvey 2009).

The characteristics of the ubiquitous nanoscale Fe-Ni-S droplets in Stardust melted grains have been investigated to infer the thermal modification history of the incident cometary particles during aerogel capture (Zolensky et al. 2006; Ishii et al. 2008; Leroux et al. 2008, 2009; Rietmeijer et al. 2008; Tomeoka et al. 2008; Velbel and Harvey 2009). These inclusions range in size from just a few nm in diameter to greater than 100 nm, with the largest examples exhibiting a Fe-Ni-core and Fe-S-mantle structure (Leroux et al. 2008). Droplets of all sizes are typically spherical, but some exhibit deformation consistent with disruption and fission (similar to that reported from microgravity experiments by Wang et al. 1990, 1994) during rotational and translational motion in the molten state prior to quenching (Velbel and Harvey 2009). The composition of the larger droplets, including the presence of trace metals, has been found to vary substantially between and also within individual samples (Leroux et al. 2008). The similarity between Fe-Ni-S inclusions in Stardust melted grains and those in chondritic aggregate IDPs has drawn attention, although the IDP inclusions are typically larger and do not exhibit core-mantle structure, suggesting different formation environments and conditions (Zolensky et al. 2006; Rietmeijer et al. 2008).

A variety of formation mechanisms have been proposed for the larger droplets with core-mantle structure. Leroux et al. (2008) suggest crystallization

sequences accounting for the range of droplet compositions, attributing the segregation of sulfide from metal to differing interfacial energies. Rietmeijer et al. (2008) hypothesize that transient extreme temperatures (>1500°C) may have facilitated the production of deep metastable eutectic compositions. Ishii et al. (2008) reproduce similar phases consisting of sulfide rims on reduced metal cores in laboratory experiments. Leroux et al. (2009) propose that, following the melting of the incident cometary material, S vaporizes and dissolves in the melted aerogel mixture and then condenses around droplets of metal that coalesced in a chemically reducing environment. There is some evidence that the cores of some larger droplets preserve cometary minerals that were not completely melted (Velbel and Harvey 2009). Abreu et al. (2011) have produced analogs of the small (<30 nm) Fe-Ni-S droplets in the laboratory by direct gas-phase condensation from a flash-cooled Fe-S-SiO-O_2 vapor.

Velbel and Harvey (2009) documented a variety of compositional parameters (of large volumes analyzed at relatively low magnifications) that appear to vary systematically with penetration distance in melted-grain allocations from Stardust Track 35. They suggested that sorting by density—an attribute indigenous to individual volumes within the incident pre-capture particle—was responsible for the observed along-track compositional variation. Several downtrack compositional trends in melted grains (e.g., increases in Fe/Mg and Fe/S with increased penetration distance; Velbel and Harvey 2009; their Figures 7, 9 and 10) suggest that the farthest-traveled melted grains may have penetrated farthest because they contained larger amounts of beads of dense, Fe-bearing minerals (e.g., Fe-Ni metals, Fe-Ni sulfides) solidified from formerly molten pre-capture metal and sulfide mineral grains, as compared with melted grains that did not penetrate as far.

The size distribution of the nanoscale Stardust Fe-Ni-S droplets may preserve information relevant to interpretation of both their composition and morphology. In general, particle size distributions reflect the equilibrium reached between aggregation and fragmentation processes (for a recent review see Villermaux 2007). The kinetic properties of aerogel capture, which result in the bulb and stylus morphology of the debris track, correspond to along-track variations in temperature, pressure, and the chemical environment of the materials that could affect the equilibrium characteristics of the population of Fe-Ni-S droplets (Zolensky et al. 2006; Rietmeijer et al. 2008; Tomeoka et al. 2008). In particular, Leroux et al. (2000) find that small (<20 nm) droplets in the Tenham (L6) chondrite are composed almost entirely of FeS, while the largest (>20 nm) droplets contain additional Fe,Ni phases.

Moreover, their average compositional analyses (their Table 3) indicate that the Fe/S ratio is higher within large droplets than in regions dominated by small droplets, while regions devoid of metal droplets contain essentially no Ni, S, or Fe outside of FeO. These results suggest that a high Fe/S ratio determined from bulk compositional analysis should be a signature of the presence of larger metal-sulfide droplets. If this relationship extends to metal-sulfide droplets in Stardust melted allocations, then the near-tripling of the Fe/S ratio in melted grains along Track 35 (Velbel and Harvey 2009; their Figure 10) might be expected to coincide with an increase in droplet size along Track 35.

The purpose of this study was to test the hypothesis that deeper penetrating melted grains in Stardust Track 35, with their higher Fe/S ratios (Velbel and Harvey 2009), contain larger metal-sulfide beads as suggested by the work of Leroux et al. (2000). The test we apply here seeks along-track variations in bead size, which would be consistent with the expectation deduced from our hypothesis. In doing so, we will produce a measurement of the droplet size distribution in each of several grains from Track 35 suitable for comparison with sulfide mineral grains in unmelted carbonaceous chondritic material. Such a detailed size distribution measurement may provide a basis for future comparisons with modeling and experimentation to isolate the effects of the capture heating and modification process and the textural properties of the pre-capture cometary material.

MATERIALS AND METHODS

A calibrated system based on astronomical image analysis is used here to automate the detection of Fe-Ni-S droplets and measure their size and geometric parameters on a suite of TEM images of five allocations extracted from various depths of a single Stardust debris track. More than 8000 droplets were identified in this sample. The data sets are then compared to establish similarities and differences between the allocations imaged that provide insight into the nature of incident pre-capture comet dust and the melted grains produced during aerogel capture.

Materials Examined

Stardust Allocations

Five melted fragments of cometary particle impact debris mixed with molten aerogel ("allocations") from Stardust Track 35 were examined; the allocations examined here are the same as those for which compositional attributes and droplet shapes were reported by Velbel and Harvey (2009). Track 35 is an 11.7 mm long aerogel capture feature from which

58 individual grains were extracted and prepared at NASA JSC during the Stardust Preliminary Examination (Zolensky et al. 2008). The terminal particle of Track 35 and the three nearest objects were lost during sample preparation, which leaves some key aspects of the nature of the incident cometary material uncertain (Velbel and Harvey 2009). As a bulbous, type-B track, it is likely that the precursor material for Track 35 was weakly aggregated and may have contained volatile elements (Trigo-Rodríguez et al. 2008). Most grains from Track 35 are classified as amorphous-rich (probably modified or formed during capture heating) and some as crystalline (formed at high nebular temperatures before capture) using X-ray diffraction and microtomography (Nakamura et al. 2008). The TOF-SIMS studies of Stephan et al. (2008) indicate that Track 35 has exceptional compositional heterogeneity relative to other Stardust tracks. The Leroux et al. (2008) investigation of Fe-Ni-S droplets included several allocations from Track 35.

Compositional and textural variations among the five allocations examined here and individual Fe-Ni-S inclusions were previously reported by Velbel and Harvey (2009). Where two different allocations close to one another along Track 35 were examined, differences in composition between neighboring allocations were commonly larger than variations between compositions of different regions within each allocation. However, an overall trend of increasing Fe relative to Mg and to S is found as a function of penetration depth and was interpreted as being due to density sorting and/or sulfur loss to the surrounding aerogel following volatilization. Allocations 16 and 24 (in the bulb of Track 35) were found to contain a greater abundance of high-Ni, low-S droplets than any other Stardust allocations, although these compositional measurements were made on the larger, multi-phase droplets not studied here. In general, Ni and S were found to be more strongly associated in Track 35 than in other tracks, where Ni was more likely to have been hosted by olivine rather than sulfides or metal.

Analytical Methods

Stardust Allocations

We acquired bright field TEM images of the five Stardust allocations using the JEOL 2200FS TEM at the Center for Advanced Microscopy at Michigan State University. Images of four non-overlapping regions were acquired from one ultramicrotome section of each allocation at 100,000× magnification (about 7.7 nm^2/px, where px is image pixels). To maximize our droplet sample size, we manually selected the regions of each section with the highest droplet density for imaging.

While four ultramicrotome sections were available for each of the five allocations, only one section from each allocation was imaged to avoid sections demonstrating high degrees of chattering. Chattering is structural damage to the section caused by spatially repetitive stress fracturing of brittle materials during ultramicrotomy (Zolensky et al. 2008). Additionally, we acquired a small number of images of these allocations at a higher magnification (800,000×, ∼0.13 nm^2/px) for the purpose of evaluating the abundance of droplets smaller than the limiting resolution of our primary dataset.

Segmentation

Detection of the Fe-Ni-S droplet sizes and measurement of their geometrical parameters (a process hereafter referred to as segmentation) can be done by visual analysis (manually), but manual measurements are time-intensive and not formally repeatable. The number of manual measurements needed for a statistical sample is prohibitive. Even a conservative estimate of the number of droplets in a relatively small ultramicrotome section (e.g., 6 μm × 6 μm × 70 nm at a density of 100 droplets/μm², as in Stodolna et al. 2009) must be greater than 3000. Moreover, manual image segmentation requires the boundaries of a droplet to be identified visually to measure its size. As we will describe in the following section, the boundaries of droplets are not always clear and it is preferable to have an automated process that can identify these boundaries according to reproducible criteria.

The segmentation of droplets in TEM images of Stardust samples presents a variety of challenges that differentiate it from common segmentation problems in sedimentology, astronomy, engineering, and other fields. These factors are enumerated below and illustrated by Fig. 1:

1. Background: In contrast to images common in sedimentology, where the grains of interest are densely packed and fill the area of the image (see, e.g., Kellerhals et al. 1975), Stardust TEM imaging exhibits complex background features. The droplets are embedded within an extremely non-uniform background due to the nature of the vesicular glassy matrix. Vesicles were probably produced by partial volatilization of sulfur and/or gas trapped in aerogel micro-pores (Tomeoka et al. 2008). EDS intensity maps illustrate the variability of Si, Ca, Al, and particularly Mg throughout the matrix (Leroux et al. 2008). The size, composition, and abundance of these vesicles may all be highly heterogeneous (Leroux et al. 2008), resulting in a background that varies in brightness (density) in an unpredictable manner. Moreover, droplets may form along vesicle boundaries as lenses (Velbel and
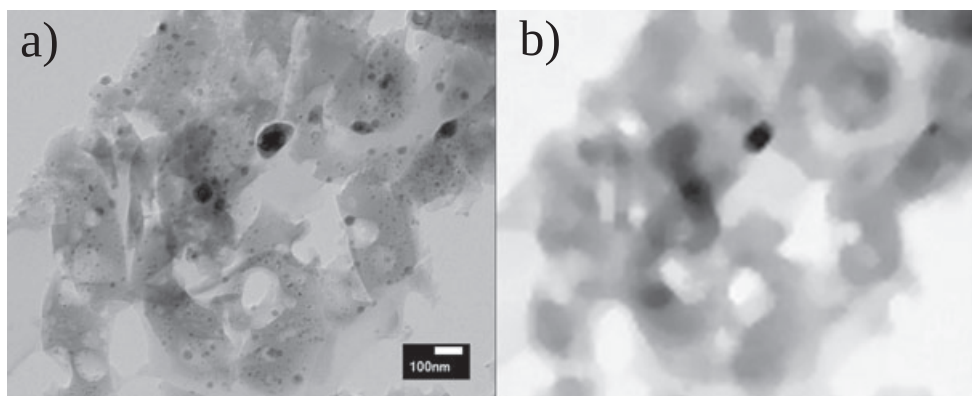
Fig. 1. a) The transmission electron microscope (TEM) image of Stardust sample C2054,0,35,52,4 ultramicrotome section #25. This is region #2 of grain 52 in our study. The features of the TEM images which present challenges to image segmentation are enumerated in the text. b) The corresponding background intensity map produced by SExtractor as described in the text.

Harvey 2009) or even appear to extend across boundaries. Sample chattering presents additional brightness discontinuities (e.g., the long bright band in Fig. 1) and the compacting of aerogel produces many regions of increased density near the sample matrix. The issue of background complexity is particularly problematic for Fourier transform methods of image segmentation, which are successful for sedimentology (e.g., Buscombe et al. 2010). As noted by Leroux et al. (2008), the non-vesicular regions of the matrix, which would be less problematic for segmentation, tend not to contain droplets.

2. Threshold: The variability of the composition of both the matrix and the inclusions themselves result in brightness differences in the TEM image that are difficult to interpret. While it would be trivial to detect dense Fe-Ni inclusions against a low-density (bright) pure-SiO_2 background, S-rich droplets can very nearly blend in with dense (dark) Mg-rich regions of the matrix. For example, for one 2.5 μm^2 image from the section of allocation #16, we find one Mg-rich region with an area of $\sim$0.07 μm^2. While regions of this density are rare, less-dense regions pose a similar (but less extreme) problem and the fact that the background-density varies widely over the image requires that the threshold adapt accordingly.

3. Crowding: While vesicles of SiO_2 glass devoid of droplets do exist among the droplet-rich regions of the sections we have imaged, some regions are characterized by highly crowded fields of Fe-Ni-S inclusions. Spheroids frequently appear to overlap through the depth of the section and while some may be physically joined (compound) droplets (as by coalescence, or inertial fission of spinning liquid into two drops, as reported from microgravity experiments by Wang et al. 1990, 1994; Velbel and Harvey 2009), others may merely border each other closely. An effective segmentation methodology must resolve joined droplets into the individual components and classify such features as one droplet or more and also define appropriate boundaries to each for size measurement.

4. Shape: While most droplets appear approximately circular in shape, assigning a precise diameter to these small inclusions is difficult to do reproducibly by eye. This is especially true where droplets are elongated along vesicle boundaries or obscured by neighboring features in dense regions. Errors or inconsistencies in assigning a size measurement could lead to a bias in the measured size distribution that is not easily quantifiable by manual segmentation methods.

5. Size: The ubiquity of extremely small droplets challenges the limit of detection. These droplets may be just a few pixels in diameter at the resolution of TEM images. Because their small size exacerbates all of the above issues, it is especially difficult to make reproducible manual measurements of these droplets.

While attempts to automate droplet segmentation are complicated by these same factors, the advantages of an automated method are the reproducibility and consistency of measurements and the opportunity for quantitative calibration.

A method to automate the segmentation of nanoscale Fe-Ni-S droplets in the TEM images was developed using astronomical image analysis tools. SExtractor 2.4.4 was implemented for object detection and IRAF 2.14.1 was used for associated image analysis tasks (Tody 1993; Bertin and Arnouts 1996). SExtractor is a software package for automated object detection, which incorporates background-subtraction, object detection, thresholding, and de-blending algorithms
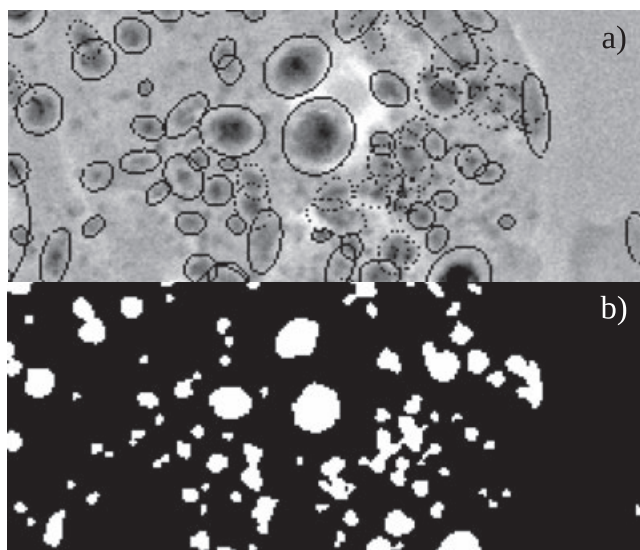
Fig. 2. An illustration of the Fe-Ni-S droplet segmentation characteristics of the optimal SExtractor configuration. a) An ellipse is drawn around each identified droplet. Dashed lines indicate when an object was deblended from neighbors in crowded regions. b) An illustration of the actual image segmentation performed by SExtractor, where the pixels attributed to each object are highlighted. Note that the size of the ellipse is drawn as larger than the area that is actually measured, as illustrated in the segmentation image.

whose parameters we have optimized to address the factors complicating segmentation enumerated above (Fig. 2). This methodology is described in detail in Appendix A.

Systematic Effects

We find that the sensitivity of our detection methodology varies as a function of the size of the droplets. Very small droplets are difficult to distinguish from the noise in the image and very large droplets are difficult to detect because they can be confused for the complex background of the vesicular matrix. In Appendix A, we describe these effects in detail and perform simulations to derive a completeness function that is used to correct this systematic variation in sensitivity.

Furthermore, we derive a correction function to account for projection effects due to the finite section thickness of our allocations. For example, a large droplet whose center falls just beyond the edge of the section will be viewed in cross-section on our TEM images, and we will therefore measure a diameter smaller than its true value. The derivation of this correction function is described in Appendix A.

Both of these corrections are plotted in Fig. 3 and are applied in combination to produce the "corrected" size distribution function we present below.
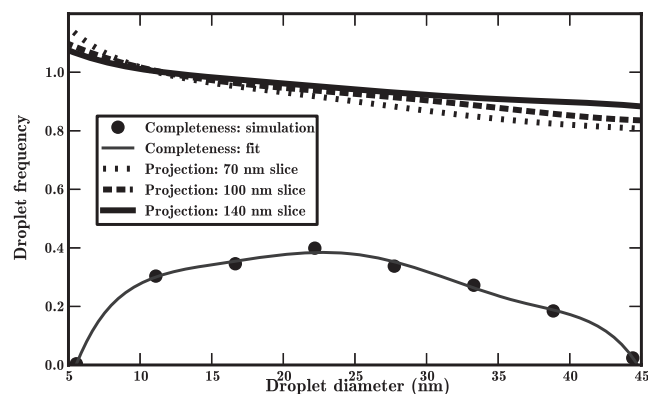

Fig. 3. The systematic correction factors applied to the measured size distribution. The lower points and polynomial fit are for the completeness function of the optimized SExtractor configuration. The completeness function equals the fraction of artificial droplets detected minus the fraction of false-positive detections. The upper lines come from the simulations modeling how the measured size distribution is effected by projection effects.

The magnification of the TEM images in our primary dataset (100,000× or ~2.8 nm/px) enforces a lower limit for the size of droplets we can detect. We do not attempt to detect droplets smaller than one pixel in radius on these images (~5 nm in diameter). Moreover, in our primary dataset, we have only limited sensitivity to droplets smaller than about 3 pixels in diameter (~5–10 nm), but we correct for this using our completeness function. However, we are able to use the high-magnification (800,000×) images to search for droplets smaller than 5 nm in diameter. The image detection methodology we have calibrated for the primary dataset is not applicable to the high magnification images because the pixel-scale area of typical droplets is enhanced by a factor of 64. We therefore identify droplets and measure their sizes manually on these images.

RESULTS

Metal-Sulfide Beads in Stardust Melted Grains

Using our automated image segmentation methodology, we detect a total of 8187 droplets in our 20 TEM images from five different allocations along Stardust Track 35. We immediately apply a very conservative cut in ellipticity to our data, setting aside all objects with ellipticity ≥0.5. This should exclude many spurious detections of non-spherical image features, such as density discontinuities on vesicle boundaries that are not properly extinguished during background subtraction. All further data analysis refers to this ellipticity-trimmed subsample of the data, which consists of a total of 6881 droplets. The counting statistics of the

Table 1. A summary of the counting statistics for detected droplets.

Depth[1] (mm)	Allocation	N[2]	Nt[3]	Droplet density[4] (10^{-6}/nm^3)	Corrected droplet density[5] (10^{-6}/nm^3)
3.51	16	1905	1656	1.64	5.17
3.67	24	1589	1319	0.93	3.24
6.08	51	1768	1451	2.05	7.19
6.55	52	1584	1224	1.73	6.31
10.38	42	1341	1161	1.64	5.81

[1]The distance of the grain from the entrance aperture along Stardust aerogel debris Track 35.
[2]N is the number of droplets detected (not corrected for the completeness function) in all four regions of that allocation's images.
[3]Nt is the number of droplets excluding those with ellipticity greater than 0.5.
[4]The droplet density (trimmed for ellipticity) obtained by dividing Nt by the thickness of the ultramicrotome section and the area imaged.
[5]The droplet density trimmed for ellipticity and corrected by the completeness and projection functions given in Fig. 3. This represents our estimate of the droplet density that would be reported by a perfect detection method.

droplet detection are summarized in Table 1. The droplet densities we find, ~ 1–2×10^{-6} nm^{-3}, are very similar to that reported by Stodolna et al. (2009; 100–200 µm^2 in a 70 nm thick ultramicrotome section). We note that if we correct the number of detected droplets based on the correction functions given in Fig. 3 (which has a typical completeness of ~ 0.3), we expect a droplet density more than three times as large. However, the completeness function is designed primarily to correct for sensitivity as a function of radius; its absolute correction level may not be well determined (see the discussion of artificial droplets in Appendix A).

The droplet size measurements are useful both with and without the correction functions. It is preferable to make comparisons between the size distributions of the five different allocations using the raw data, before the correction has been applied. However, in comparing the size distribution with the literature and to draw physical inferences from it, the correction must be applied to recover the correct shape of the distribution function.

Uncorrected Droplet Size Distributions

The size distribution histograms for each allocation before correction are presented in Fig. 4. Each droplet size distribution is produced by collecting all the droplet size measurements from the four regions imaged. We combine all the regions because the normalized cumulative size distributions of droplets from different regions within individual allocations are typically highly consistent. We illustrate this consistency in Fig. 5 and quantify it by performing the two-sample Kolmogorov-Smirnov (KS) test on each of the six pairs of regions within each of the five allocations. Of these 30 tests, only four yielded P-values less than 0.01, indicating a strongly significant difference. However, even for regions which have size distributions that are significantly different according to the KS test, this difference is small; the difference in the mean droplet diameter is never as large as 3 nm.
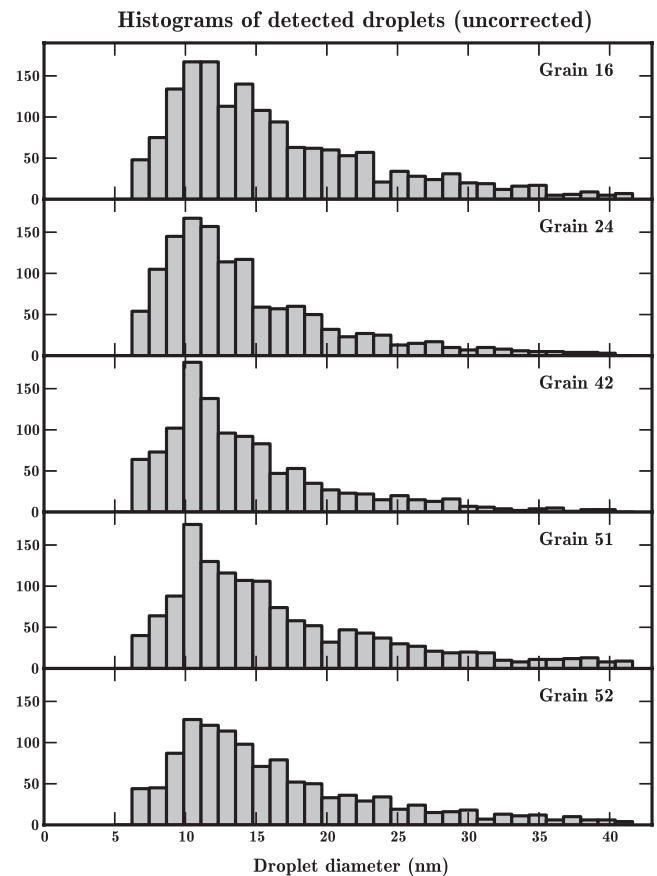

Fig. 4. Fe-Ni-S droplet size distributions, not corrected by the completeness function given by Fig. 3.

From Fig. 4, it appears that the size distributions for all five allocations are similar in that they are unimodal with a mean diameter near 15 nm, a standard deviation near 7, and an exponentially decaying large-diameter tail. We will discuss the size distribution in more detail in the following section, where the correction has been applied.

We examine the cumulative distribution functions of each allocation (Fig. 6). This allows investigation of the
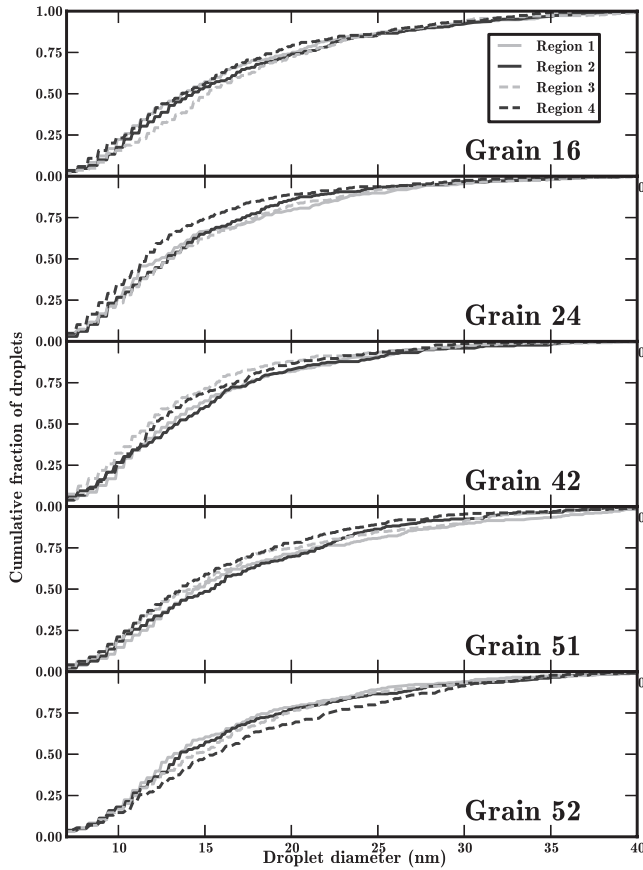
Fig. 5. Cumulative size distribution functions for Fe-Ni-S droplets in each region imaged in each grain (not corrected for completeness or projection).
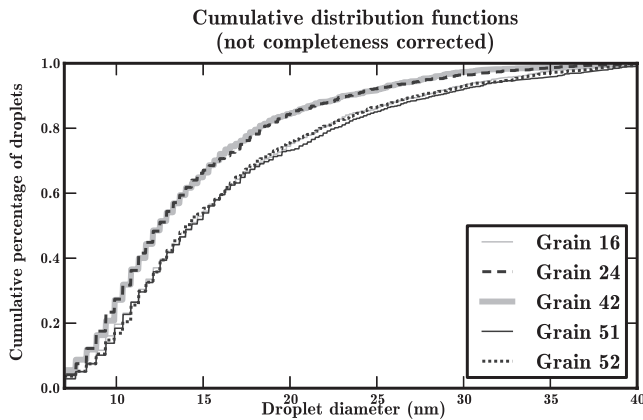

Fig. 6. Cumulative size distribution functions for Fe-Ni-S droplets in each grain (not corrected for completeness or projection).

along-track variation in the droplet size distribution by inspecting the moments of the distribution (mean, variance, skewness, and kurtosis) as a function of debris track depth (Fig. 7), and by performing the KS test
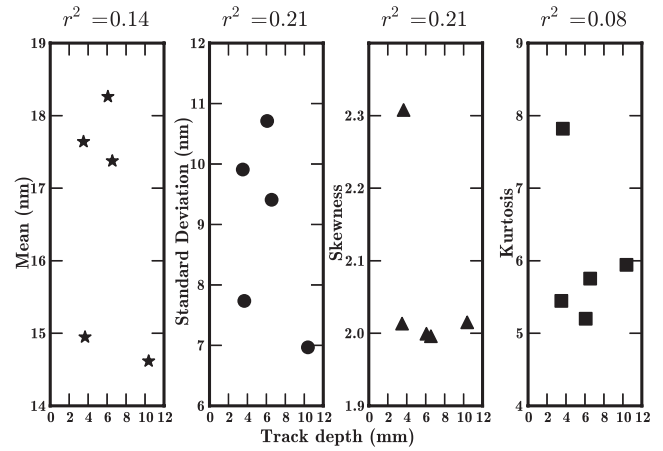

Fig. 7. The moments of the droplet diameter size distribution (not corrected for completeness and projection) as a function of depth along Stardust aerogel debris Track 35. The Pearson coefficient of determination (r^2) for the correlation of the moments with track depth is given above the plot.

(Table 2). Refer to Table A1 or Velbel and Harvey (2009) for the along-track depth of each allocation. Fig. 7 illustrates that there are no clear trends for any of the moments along the depth of the track. The coefficient of determination (r^2) value for each moment as a function of penetration depth is ≤0.25.

Corrected Droplet Size Distributions

Next we attempt to determine the intrinsic droplet size distribution corrected for the systematic effects of our detection methodology and suitable for comparison with exterior datasets. For the uncorrected droplet size distributions, we argued that the size distribution of droplets does not vary significantly among allocations in our sample distributed along Track 35 (this will be discussed further in the following section); here, we operate on the aggregated statistics of droplets detected in all allocations. We then correct for the detection sensitivity by multiplying the distribution by the inverse of the completeness and projection correction functions (see Appendix A and Fig. 3).

The final, corrected size distribution for droplets from all grains is presented in Fig. 8. Like the uncorrected distributions of the individual allocations, it is unimodal within the size range sampled (∼7–40 nm). The existence of two bins for sizes < 10 nm that have fewer counts than the peak indicates a maximum (mode) in the size distribution at ∼11 nm. The corrected distribution has a mean at 17.1 nm, median at 14.1 nm, standard deviation of 8.3 nm, skewness of 1.2, and kurtosis of 0.7. While the mean, median, and standard deviation of the corrected and uncorrected distributions are equal within ∼1 nm, we note that the skewness of the uncorrected distribution is

Table 2. Two-sample Kolmogorov-Smirnof (KS) statistics[1] for the droplet sizes measured from all five allocations (not completeness corrected).

	Allocation 16	Allocation 24	Allocation 42	Allocation 51	Allocation 52
Allocation 16		0.142	0.143	0.030	0.025
Allocation 24	0.000		0.025	0.155	0.131
Allocation 42	0.000	0.844		0.147	0.136
Allocation 51	0.496	0.000	0.000		0.039
Allocation 52	0.749	0.000	0.000	0.256	

[1]The KS D values are given above the diagonal and the corresponding P-value is given below the diagonal. The D statistic reflects that maximum distance between the cumulative frequency distributions of the two size distributions, while the P-value reflects the probability that a discrepancy as large as D would be produced if you were to randomly draw the sampled grain sizes from the same distribution. A P-value ≤ 0.05 indicates that the two size distributions compared are different at a statistically significant level.
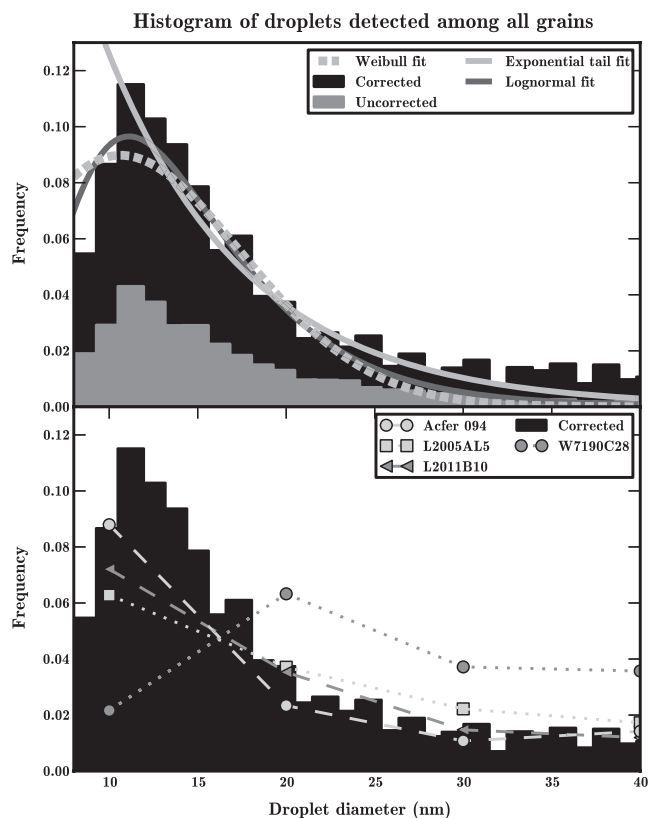

Fig. 8. Top: Fe-Ni-S droplet size distributions, both before (gray) and after (black) correction by the completeness function given by Fig. 3. Lines are drawn for the best fit lognormal and Weibull distributions for the entire histogram and the best fit exponential for droplets larger than about 10 nm (the coarse tail of the distribution). Bottom: Comparison with the size distributions measured for IDPs and the Acfer meteorite (lines) by Sekigawa and Keller (2010). The corrected size distribution has been replotted for clarity and is identical to the top figure.

2.2 and its kurtosis is 6.5. Without the completeness correction, the distribution is more peaked because objects near the mode are more easily detected. For comparison, the droplet size distributions of the three IDPs and the Acfer 094 chondrite (Sekigawa and Keller 2010) are also plotted on Fig. 8.

High Magnification Images

We search for a population of droplets below the limiting resolution of our primary dataset on our high-magnification images. From images of three regions of allocations 24 and 48 ($\sim$0.13 μm^2 total imaging area), we identify 148 droplets with diameters ranging from 3.3 to 41 nm. These droplets demonstrate a unimodal size distribution with a mode near $\sim$10 nm, reflective of the distribution we measure from the primary dataset. Only 7% of the droplets identified on the high-magnification image have diameters below the limiting resolution of the primary dataset (<5 nm). Our observations from the high-magnification images indicate that the <5 nm-sized droplets represent an extreme tail of the primary droplet size distribution. Consequently, the size distribution measured from our primary dataset (which already samples below the mode of this distribution) is sufficient for characterizing the droplet size distribution. Because the instrument time required to complete a survey of this type grows with the square of the magnification, we do not advise acquiring large quantities of images at this high magnification.

DISCUSSION

Metal-Sulfide Beads in Stardust Melted Grains

The objects referred to here as (formerly molten) droplets or beads apparently solidified from drops of molten metal-sulfide material dispersed in molten silica. The larger (>40 nm) droplets consist of multiple mineral phases, with Fe-Ni metal or sulfide in the interior and Ni-free iron monosulfide in the shells; the smaller droplets investigated in this study appear mostly to consist of a single phase (Zolensky et al. 2006; Leroux et al. 2008; Velbel and Harvey 2009). Along-track variation in droplet size distributions is minor. For the first part of this discussion, the aggregate droplet size distribution of the entire Track 35 data set is treated as a single distribution. In the next section, the minor variations among allocations are discussed. Comparison

with size distributions of sulfides in IDPs and C-chondrites then follows.

Overall Droplet Size Distribution

The size distribution of Stardust Track 35 metal-sulfide beads (Fig. 8) is dominated by a mode near 11 nm, but is coarse-skewed, with a mean of 16.7 nm. This section explores the processes acting on the molten droplets that might have given rise to the observed size distribution. However, additional work beyond the scope of the present observational study would be required to uniquely associate characteristics of the measured droplet size distribution with the underlying physical processes responsible for its creation.

The observed Stardust Fe-Ni-S droplet size distribution is predominantly unimodal (Fig. 8). There is a possible incipient coarse mode near 16 nm, which is also suggested on several individual (uncorrected) allocation histograms (Fig. 4, particularly grains 16 and 52). Coarse modes or "shoulders" of the size distribution can be produced by enlarging processes such as diffusional growth and Ostwald ripening (Ratke 1988, 1995; Ratke and Diefenbach 1995). In turbulent dispersions, the strength of the coarse mode implies a limit to the coalescence rate of liquid particles (Coulaloglou and Tavlarides 1977; Sechremeli et al. 2006). However, the timescale for aerogel capture and cooling of Stardust aerogel-capture melts (heating pulse duration of microseconds; Trigo-Rodríguez et al. 2008) is much shorter than the timescales applied to produce an equilibrium droplet size distribution in turbulent suspensions ($\sim$90 min for $\sim$100 µm sized droplets; Sechremeli et al. 2006). Stretching and breaking of droplets can produce smaller droplets from larger ones. When a droplet breaks into two smaller droplets in a turbulent dispersion, the material transiently present as the filament connecting the two separating droplets often becomes a spray of "daughter" droplets that constitute a second, fine mode (Stone 1994; Desnoyer et al. 2003). The absence of a second fine mode in the Stardust Track 35 droplet size distribution, even among droplets identified in our higher magnification images, suggests that such breakage processes were not a widespread aspect of aerogel capture modification. While the shapes of some large compound droplets have been interpreted as resulting from drop-stretching (Leroux et al. 2008, Fig. 11c; Velbel and Harvey 2009, Fig. 5), their rarity supports this inference.

We first model the size distribution with the lognormal function, which is characteristic of processes including sequential cascading fragmentation and coalescence and results physically from the Central Limit Theorem (Granqvist and Buhrman 1976; Villermaux 2007). The best-fit lognormal function, plotted in Fig. 8, has the following parameters: statistical median of 13.2 nm and geometric standard deviation of 1.51. The best-fit function is adequate for indicating the mode and width of the function and its behavior at fine scales, beneath the mode. However, the best-fit function underestimates the peakedness of the distribution and does not reproduce its coarse tail ($>$25nm).

Next, we fit the coarse tail of the distribution ($>$11 nm) with the exponential function representative of scale-invariant fragmentation (Villermaux 2007). The best-fit function has an exponent of -0.12x, where x is the droplet diameter in nm. The exponential function is well-suited for describing the measured size distribution from its peak near 11 nm to relatively far out into the coarse tail, $\sim$30 nm. Of course, the exponential does not describe the maximum in the distribution or the distribution's behavior at small sizes below the mode.

Finally, we fit the full size-distribution with the Rosin-Rammler (a.k.a. Weibull) distribution, which combines a power law and exponential dependence on particle size to provide a description of fragmentation processes that is arguably more robust than the lognormal function (see e.g., Brown and Wohletz 1995). The best-fit Rosin-Rammler distribution (shape parameter k = 2.2, scale parameter λ = 14.0 nm) is even more grievous than the lognormal function at underestimating the peakedness of the distribution and also over-estimates the number of droplets with small diameter. Its behavior at $>$15 nm is nearly identical to the lognormal distribution.

The overall textural appearance of the now-solidified metal-sulfide droplets dispersed in quenched silica glass resembles the production of ultra-fine metal droplets via inert-gas evaporation. This method produces spherical droplets with log-normal size distributions similar to that of the Stardust Fe-Ni-S droplets (Granqvist and Buhrman 1976). For example, Granqvist and Buhrman (1976) produced Mg droplets with a median diameter of $\sim$15 nm using an argon vapor with a pressure of $\sim$2 torr and a temperature of $\sim$900 K. They find that the geometric standard deviations of 1.36–1.60 (as we report above) are characteristic of inert-gas exaporation, while chemical vapor deposition techniques for producing colloids and coalescing islands in discontinuous films produce significantly more narrow size distributions. For comparison, Abreu et al. (2011) produce nanophase sulfide compounds resembling Stardust droplets using a dust generator operating at $\sim$90 Torr and a $\sim$1500 K flame in an H_2 atmosphere, that bears some similarities to inert-gas evaporation. However, they determined only the size range, not the size distribution, of their experimental products. While there are significant differences between these methods and inert-gas evaporation, further dust generator experimentation may make it possible to build up something like the sintering temperature-grain size relation (Siegal 1991). In this way,

one could determine the parameters (e.g., temperature, exposure duration, pressure, etc.) necessary to closely reproduce the observed Stardust size distribution.

During aerogel capture, a subset of the Stardust grains reached temperatures sufficient to melt their minerals completely (e.g., Zolensky et al. 2006; Leroux et al. 2008; Velbel and Harvey 2009), and some fraction of the incident particles reached vaporization temperatures (e.g., Noguchi et al. 2007; Roskosz et al. 2008; Trigo-Rodríguez et al. 2008; Dominguez 2009). Vapor-related processes can produce droplets with size distributions (Granqvist and Buhrman 1976) similar to those reported here, and Abreu et al. (2011) experimentally produced beads in the same size range as observed here. However, vaporization–condensation processes are not a unique match to the Stardust droplet size distribution reported here. Other examples of similar size distributions produced by laboratory techniques include the dispersed microstructure of immiscible alloys experimentally solidified under microgravity conditions lacking gravitationally influenced convection and sedimentation effects that would separate more-dense from less-dense phases (Ratke 1988; Andrews et al. 1993; Ratke and Diefenbach 1995) and droplets formed during liquid atomization and production of sprays (Babinsky and Sojka 2002). However, the larger size regime ($\sim$1–100 μm) of these experiments could limit the relevance of this literature for comparison with the nanometer-sized Stardust particles. For example, the inherent discretization of the growth of nanoparticles causes Ostwald ripening to produce significantly more narrow and faster growing size distributions than predicted by the classical Lifshitz–Slyozov–Wagner (LSW) population balance model for particle growth (Mantzaris 2005; see their Fig. 7a). Moreover, the percentage of particles' constituent atoms which lie on the grain boundary of the droplet can rise sharply for droplets < 100 nm in size, increasing the role of interface structures (Siegal 1991).

Along-Track Variation in Droplet Size Distributions among Individual Allocations

Because the Fe/S ratio increases with the size of metal-sulfide droplets in the Tenham (L6) chondrite (Leroux et al. 2000) and because the Fe/S ratio nearly triples throughout the depth of Stardust Track 35 (Velbel and Harvey 2009), we have hypothesized that the mean droplet diameter should increase with track depth in the five allocations studied here. We test this hypothesis by plotting the moments (mean, standard deviation, skewness, and kurtosis) of the size distribution as measured from TEM images from each allocation as a function of the penetration depth (Fig. 7). However, the correlation with penetration depth is very low (r^2 < 0.25 for all parameters), indicating that there are no significant trends along the track. For comparison, Velbel and Harvey (2009) reported that Fe/S and (Fe + Ni)/S ratio both increase as a function of track depth, with r^2 = 0.85 and 0.84, respectively.

Position along the debris track is therefore not a good predictor of the size distribution of droplets in any two allocations. For example, allocations 16 and 24, the allocations nearest to the entry aperture and nearest to one another within the bulb of the debris track, demonstrate a 30% difference in the standard deviation of their size distributions. The cumulative distribution functions of Fig. 6 demonstrate that the shape of the size distribution is similar in all five allocations, but hint that in detail, there are two different classes of distributions. The cumulative droplet size distributions of allocations 24 and 42 (located in the bulb and nearest to the track terminus, respectively) are much more similar to each other, and slightly finer-grained, than to the distributions of allocations 16 (located in the bulb closest to the entry aperture), 51, and 52 (located near each other at the bulb/stylus transition). The KS statistics given in Table 2 quantify and support this result: the allocations with size distributions that appear qualitatively similar have KS test P-values > 0.05 and those that appear different have P-values < 0.05. Interestingly, the allocations which contained extreme fractions of high-Ni, low-S droplets (allocations 16 and 24, Velbel and Harvey 2009) do not fall in the same textural class. Fragments of incident particles that melted to produce emulsions with similar droplet size distributions were not systematically distributed along the track. Instead, fragments that melted to produce similar droplet size distributions are distributed to different penetration depths along Track 35 (e.g., 42 versus 51 and 52; 24 versus 51 and 52), and fragments that melted to produce different droplet size distributions are immediately adjacent to one another (16 and 24).

Several compositional abundance ratios of whole-allocations (Fe/S, Fe/Mg, S/Fe, S/Ni as measured by TEM-EDS) vary along track in Track 35; compositions can vary widely among different analyzed areas of the same allocation; and adjacent allocations exhibit distinct compositional ranges (Velbel and Harvey 2009). However, texturally distinct allocations 24 and 42 do not group distinctly from 16, 51, and 52 in the TEM-EDS compositional analyses of the same allocations as reported by Velbel and Harvey (2009). Within- and between-allocation variations in compositional and textural attributes beyond those loosely correlated with penetration depth (Velbel and Harvey 2009) may be consequences of within- and between-allocation variations in compositional and textural heterogeneities among different volumes of the incident comet-dust particles. Capture-melting of compositionally and

texturally different incident fragments produced compositionally and texturally different melted grains. As with the preservation of "ghost grains" (Leroux et al. 2008), variable compositional (Velbel and Harvey 2009) and textural (this study) products of capture-melting appear to preserve compositional and textural attributes of the incident fragments, rather than representing quenching of well-mixed and homogenized capture-produced melt.

Candidates for Incident-Particle Precursors of Melted Grains: Sulfides in Interplanetary Dust Particles and Primitive Carbonaceous Chondrites

Iron sulfides in IDP L2011A9 are somewhat larger than sulfides in Stardust Track 44 (Rietmeijer 2009). Overlap of compositions between the smaller grains among Stardust samples and some grains in the IDP led Rietmeijer (2009) to conclude that the smaller IDP grains were the most likely to have reacted with the silica aerogel to produce the S-rich subset of Stardust Fe-Ni-S compounds. From this, Sekigawa and Keller (2010) further attributed to Rietmeijer (2009) the inference "that nanometer-size sulfides in Stardust melted grains are melt products of similar-size sulfides in IDP-like comet dust."

Sekigawa and Keller (2010) determined chemical compositions and particles sizes of sulfides in matrix fragments of the primitive carbonaceous chondrite Acfer 094 (Nguyen et al. 2007) and three CP IDPs (Dai and Bradley 2001; Keller and Messenger 2007) by TEM as possible candidate parent materials of sulfides and associated minerals in Stardust samples. The chondrite Acfer 094 and two of the three IDPs, L2011B10 and L2005AL5, exhibit approximately log-normal size distributions, with modes between ∼10 and 20 nm (Sekigawa and Keller 2010; their Figure 2). The third IDP, W7190C28, contains a much wider variation in sizes, with few small grains, and more grains and polycrystalline sulfide aggregates in the larger size fraction. Sekigawa and Keller (2010) attribute the coarser sulfide grains in W7190C28 to annealing and growth of sulfide grains prior to accretion in the solar nebula, consistent with previous similar inferences by Nguyen et al. (2007) about silicate aggregates in the same IDP.

The coarse-skewed, predominantly unimodal (mode ≈ 11 nm, mean = 16.7 nm, median = 13.6 nm, standard deviation = 9.3 nm) Stardust Track 35 droplet size distribution resembles those reported by Sekigawa and Keller (2010) from carbonaceous chondrite Acfer 094, and CP IDPs that escaped nebular annealing of sulfides. This similarity is illustrated in Fig. 8, although we note that the droplet detection methodology applied by Sekigawa and Keller (2010) was different than that

implemented here. The conservative explanation is that the size distribution of metal-sulfide beads in quenched melted-grain emulsions is inherited from the size distribution of sulfide mineral grains in comet-dust particles of chondritic character, as suggested by Rietmeijer (2009). The slightly smaller modal size of the Stardust beads suggests minor loss of mass relative to the sizes of sulfides in Acfer 094 and CP IDPs during aerogel capture. However, this comparison is limited by the loss of the terminal particle of Track 35, which prevents the determination of the bulk composition of the incident cometary particle that produced the droplets examined in this study (Velbel and Harvey 2009).

The Stardust Track 35 droplet size distribution determined here is also similar to that reported by Leroux et al. (2000) from silicate-dominated shock melts with quenched metal-sulfide objects in a shocked ordinary-chondrite. In the Tenham (L6) chondrite, Leroux et al. (2000) find an exponentially decreasing frequency of Fe-rich globules with diameters > 10 nm. The size distribution of sulfide mineral grains in unshocked Tenham is unknown, so the possibility that droplet size distributions are inherited during shock melting of Tenham, in a manner similar to that proposed here for inheritance of Stardust droplet sizes from the sulfide grain sizes of incident chondritic matter, cannot be refuted on the basis of presently available evidence.

Future Work

We have found that one important aspect of the capture modification process (penetration depth and associated compositional differentiation) is not responsible for systematic modification of the nanoscale metal-sulfide droplet size distribution in Stardust samples from Track 35. Additionally, we have demonstrated an observational similarity between the droplet size distributions found in Stardust grains, IDPs, primitive carbonaceous chondrites, and shocked ordinary chondrites. This constraint on the effects of capture modification and textural similarly suggests, but cannot confirm, the inference that the droplet sizes are inherited from pre-capture cometary materials that resemble IDPs and chondrites.

Additional modeling or experimentation is required to address the effect that different modification processes would have on the droplet size distribution, or to quantitatively compare the droplet size distribution found in nanoscale droplet formation experiments (e.g., Abreu et al. 2011) with that measured here for Stardust samples. We suggest that future authors determine droplet size distributions from controlled experiments using methods similar to that outlined in our Appendix A, and compare their results with the distribution measured here (Fig. 8) to identify how formation/

modification conditions manifest themselves in metal-sulfide textures. In particular, careful measurement of the size distribution of Fe-Ni-S droplets that result from a suite of dust generator experiments performed while systematically varying the temperature, pressure, and other parameters could be used to determine the precise conditions present in Stardust melted grains during capture modification.

SUMMARY AND CONCLUSIONS

Size distributions of metal-sulfide beads quenched after melting during aerogel capture in five allocations from various places from the bulb to near the terminus of the stylus of aerogel Track 35 were determined from TEM images. Size distributions of droplets are consistent within different regions imaged in individual allocations. The size distribution of all droplets detected among the five allocations is unimodal with a mode near 11 nm, a mean near 17 nm, and a standard deviation of about 9 nm. The distribution is coarse-skewed and leptokurtic. A lognormal function provides a reasonable description of the distribution, but does not reproduce either its peakedness or its coarse tail, which is better fit by an exponential function.

The size distribution is qualitatively similar among all five allocations studied. However, the distribution is not entirely consistent between allocations, with agreement between some and disagreement between others quantified at a statistically significant level (Table 2). However, these discrepancies are apparently functions of some property other than penetration distance along the capture track. While a variety of processes, such as gas-phase condensation, can successfully explain the observed properties of Stardust droplets, none produce size distributions that uniquely, exclusively match the observed Stardust droplet size distributions reported here. Several lines of evidence suggest that droplet size distributions are unrelated to capture modification processes, and rather reflect a preserved consequence of heterogeneity in the incident cometary material.

The textures of individual metal-sulfide droplets dispersed throughout silica-rich material, and the droplet size distributions of large populations of droplets, can be interpreted as indicating that a compositionally heterogeneous melt (Leroux et al. 2008; Stephan et al. 2008) formed by rapid melting of fine-grained compositionally heterogeneous comet dust. The similarity of the mode (near 10 nm) and exponential coarse tail are consistent with direct inheritance of the Stardust droplet size distribution in quenched melted-grain emulsions from the size distributions of unmelted sulfide mineral grains in incident comet-dust particles of chondritic character, such as CP IDPs and the matrix of the unique carbonaceous chondrite Acfer 094. The process responsible for producing the metal-sulfide size distribution acted on the pre-capture comet particle, not during capture in aerogel, such that the extracted allocations largely preserve the pre-capture size distribution of metal-sulfides in the incident comet-dust particle.

Editorial Handling—Dr. Bradley De Gregorio

REFERENCES

Abreu N. M., Rietmeijer F. J. M., and Nuth J. A. 2011. Understanding the mechanisms of formation of nanophase compounds from Stardust: Combined experimental and observational approach. *Meteoritics & Planetary Science* 46:1082–1096.

Anderson W. W. and Ahrens T. J. 1994. Physics of interplanetary dust capture via impact into organic polymer foams. *Journal of Geophysical Research* 99:2063–2071.

Andrews J. B., Schmale A. L., Dwyer Z. B., Moss C. B., and Hayes L. J. 1993. Solidification in immiscible alloys. *Advances in Space Research* 13:229–234.

Babinsky E. and Sojka P. E. 2002. Modeling drop size distributions. *Progress in Energy and Combustion Science* 28:303–329.

Bastien R., Messenger K., See T. H., Warren J. L., and Zolensky M. E. 2006. *Stardust Sample Catalog*. http://curator.jsc.nasa.gov/stardust/sample_catalog. Accessed July 6, 2011.

Bertin E. and Arnouts S. 1996. SExtractor: Software for source extraction. *Astronomy & Astrophysics Supplement* 317:393–404.

Bradley J. P., Jones A. P., and Brownlee D. E. 2009. Insight from the unexpected. *Meteoritics & Planetary Science* 44:1403–1405.

Brown W. K. and Wohletz K. H. 1995. Derivation of the Weibull distribution based on physical principles and its connection to the Rosin–Rammler and lognormal distributions. *Journal of Applied Physics* 78:2758–2763.

Brownlee D. E., Tsou P., Anderson J. D., Hanner M. S., Newburn R. L., Sekanina Z., Clark B. C., Hörz F., Zolensky M. E., Kissel J., McDonnell J. A. M., Sandford S. A., and Tuzzolino A. J. 2003. Comet and interstellar dust sample return mission. *Journal of Geophysical Research* 108:SRD 1-1, CiteID 8111, DOI 10.1029/2003JE002087

Brownlee D., Tsou P., Aléon J., Alexander C. M. O'D., Araki T., Bajt S., Baratta G. A., Bastien R., Bland P., Bleuet P.,

Borg J., Bradley J. P., Brearley A., Brenker F., Brennan S., Bridges J. C., Browning N. D., Brucato J. R., Bullock E., Burchell M. J., Busemann H., Butterworth A., Chaussidon M., Cheuvront A., Chi M., Cintala M. J., Clark B. C., Clemett S. J., Cody G., Colangeli L., Cooper G., Cordier P., Daghlian C., Dai Z., D'Hendecourt L., Djouadi Z., Domínguez G., Duxbury T., Dworkin J. P., Ebel D.S., Economou T. E., Fakra S., Fairey S. A. J., Fallon S., Ferinni G., Ferroir T., Fleckenstein H., Floss C., Flynn G., Franchi I. A., Fries M., Gainsforth Z., Gallien J.-P., Genge M., Gilles M. K., Gillet P., Gilmour J., Glavin D. P., Gounelle M., Grady M. M., Graham G. A., Grant P. G., Green S. F., Grossemy F., Grossman L., Grossman J. N., Guan Y., Hagiya K., Harvey R., Heck P., Herzog G. F., Hoppe P., Hörz F., Huth J., Hutcheon I. D., Ignatyev K., Ishii H., Ito M., Jacob D., Jacobsen C., Jacobson S., Jones S., Joswiak D., Jurewicz A., Kearsley A. T., Keller L. P., Khodja H., Kilcoyne A. L. D., Kissel J., Krot A., Langenhorst F., Lanzirotti A., Le L., Leshin L. A., Leitner J., Lemelle L., Leroux H., Liu M.-C., Luening K., Lyon I., MacPherson G., Marcus M. A., Marhas K., Marty B., Matrajt G., McKeegan K., Meibom A., Mennella V., Messenger K., Messenger S., Mikouchi T., Mostefai S., Nakamura T., Nakano T., Newville M., Nittler L. R., Ohnishi I., Ohsumi K., Okudaira K., Papanastassiou D. A., Palma R., Palumbo M. E., Pepin R. O., Perkins D., Perronnet M., Pianetta P., Rao W., Rietmeijer F. J. M., Robert F., Rost D., Rotundi A., Ryan R., Sandford S. A., Schwandt C. S., See T. H., Schlutter D., Sheffield-Parker J., Simionovici A., Simon S., Sitnitsky I., Snead C. J., Spencer M. K., Stademann F. J., Steele A., Stephan T., Stroud R., Susini J., Sutton S. R., Suzuki Y., Taheri M., Taylor S., Teslich N., Tomeoka K., Tomioka N., Toppani A., Trigo-Rodríguez J. M., Troadec D., Tsuchiyama A., Tuzzolino A. J., Tyliszczak T., Uesugi K., Velbel M., Vellenga J., Vicenzi E., Vincze L., Warren J., Weber I., Weisberg M., Westphal A. J., Wirick S., Wooden D., Wopenka B., Wozniakiewicz P., Wright I., Yabuta H., Yano H., Young E. D., Zare R. N., Zega T., Ziegler K., Zimmerman L., Zinner E., and Zolensky M. 2006. Comet 81P/Wild 2 under a microscope. *Science* 314:1711–1716.

Burchell M. J., Graham G., and Kearsley A. 2006. Cosmic dust collection in aerogel. *Annual Reviews of Earth and Planetary Sciences* 34:385–428.

Burchell M. J., Fairey S. A. J., Wozniakiewicz P., Brownlee D. E., Hörz F., Kearsley A. T., See T. H., Tsou P., Westphal A., Green S. F., Trigo-Rodríguez J. M., and Domínguez G. 2008. Characteristics of cometary dust tracks in Stardust aerogel and laboratory calibrations. *Meteoritics & Planetary Science* 43:23–40.

Burchell M. J., Foster N. J., Ormond-Prout J., Dupin D., and Armes S. P. 2009. Extent of thermal ablation suffered by model organic microparticles during aerogel capture and hypervelocities. *Meteoritics & Planetary Science* 44:1407–1419.

Burnett D. S. 2006. NASA returns rocks from a comet. *Science* 314:1709–1710.

Buscombe D., Rubin D. M., and Warrick J. A. 2010. A universal approximation of grain size from images of noncohesive sediment. *Journal of Geophysical Research* 115:F02015.

Coulaloglou C. and Tavlarides L. 1977. Description of interaction processes in agitated liquid-liquid dispersions. *Chemical Engineering Science* 32:1289–97.

Dai Z., and Bradley J. P. 2001. Iron-nickel sulfides in anhydrous interplanetary dust particles. *Geochimica et Cosmochimica Acta* 65:3601–3612.

Desnoyer C., Masbernat O., and Gourdon C. 2003. Experimental study of drop size distributions at high phase ratio in liquid-liquid dispersions. *Chemical Engineering Science* 58:1353–1363.

Dominguez G. 2009. Time evolution and temperatures of hypervelocity impact-generated tracks in aerogel. *Meteoritics & Planetary Science* 44:1431–1443.

Ebel D. S., Greenberg M., Rivers M. L., and Newville M. 2009. Three-dimensional textural and compositional analysis of particle tracks and fragmentation history in aerogel. *Meteoritics & Planetary Science* 44:1445–1463.

Eisenhour D. D. 1996. Determining chondrule size distributions from thin-section measurements. *Meteoritics & Planetary Science* 31:243–248.

Flynn G. J., Bluet P., Borg J., Bradley J. P., Brenker F. E., Brennan S., Bridges J., Brownlee D. E., Bullock E. S., Burghammer M., Clark B. C., Dai Z. R., Daghlian C. P., Djouadi Z., Fakra S., Ferroir T., Floss C., Franchi I. A., Gainsforth Z., Gallien J.-P., Gillet P., Grant P. G., Graham G. A., Green S. F., Grossemy F., Heck P. R., Herzog G. F., Hoppe P., Hörz F., Huth J., Ignateyev K., Ishii H. A., Janssens K., Joswiak D., Kearsley A. T., Khodja H., Lanzirotti A., Leitner J., Lemelle L., Leroux H., Luening K., MacPherson G. J., Marhas K. K., Marcus M. A., Matrajt G., Nakamura T., Nakamura-Messenger K., Nakano T., Newville M., Papanastassiou D. A., Piantetta P., Rao W., Riekel C., Rietmeijer F. J. M., Rost D., Schwandt C. S., See T. H., Sheffield-Parker J., Simionovici A., Sitnitsky I., Snead C. J., Stadermann F. J., Stephan T., Stroud R. M., Susini J., Suzuki Y., Sutton S. R., Taylor S., Teslich N., Troadec D., Tsou P., Tsuchiyama A., Uesugi K., Vekemans B., Vicenzi E. P., Vincze L., Westphal A. J., Wozniakiewicz P., Zinner E., and Zolensky M. E. 2006. Elemental compositions of comet 81P/Wild 2 samples collected by Stardust. *Science* 314:1731–1734.

Fries M., Burchell M., Kearsley A., and Steele A. 2009. Capture effects in carbonaceous material: A Stardust analog study. *Meteoritics & Planetary Science* 44:1465–1474.

Granqvist C. G. and Buhrman R. A. 1976. Ultrafine metal particles. *Journal of Applied Physics* 47:2200–2219.

Hörz F., Bastien R., Borg J., Bradley J. P., Bridges J. C., Brownlee D., Burchell M. J., Chi M., Cintala M. J., Dai Z. R., Djouadi Z., Domínguez G., Economou T. E., Fairey S. A. J., Floss C., Franchi I. A., Graham G. A., Green S. F., Heck P., Hoppe P., Huth J., Ishii H., Kearsley A. T., Kissel J., Leitner J., Leroux H., Marhas K., Messenger K., Schwandt C. S., See T. H., Snead C. J., Stademann F. J., Stephan T., Stroud R., Teslich N., Trigo-Rodríguez J. M., Tuzzolino A. J., Troadec D., Tsou P., Warren J., Westphal A. J., Wozniakiewicz P., Wright I., and Zinner E. 2006. Impact features on Stardust: Implications for comet 81P/Wild 2 dust. *Science* 314:1716–1719.

Ida Y., Tsuchiyama A., Kadano T., Sakamoto K., Nakamura T., Uesugi K., Nakano T., and Zolensky M. E. 2010. Three-dimensional shapes and Fe contents of Stardust impact tracks: A track formation model and estimation of comet Wild 2 coma dust particle densities. *Meteoritics & Planetary Science* 45:1302–1319.

Ishii H. A., Bradley J. P., Dai Z. R., Chi M., Kearsley A. T., Burchell M. J., Browning N. D., and Molster F. 2008a.

Comparison of comet 81P/Wild 2 dust with interplanetary dust from comets. *Science* 319:447–450.

Ishii H. A., Brennan S., Bradley J. P., Luening K., Ignatyev K., and Pianetta P. 2008b. Recovering the elemental composition of comet Wild 2 dust in five Stardust impact tracks and terminal particles in aerogel. *Meteoritics & Planetary Science* 43:215–231.

Jacob D., Stodolna J., Leroux H., Langenhorst F., and Houdellier F. 2009. Pyroxenes microstructures in comet 81P/Wild 2 terminal Stardust particles. *Meteoritics & Planetary Science* 44:1475–1488.

Joswiak D. J., Brownlee D.E., Matrajt G., Westpha A. J., and Snead C. J. 2009. Kosmochloric Ca-rich pyroxenes and FeO-rich olivines (Kool grains) and associated phases in Stardust tracks and chondritic porous interplanetary dust particles: Possible precursors to FeO-rich type II chondrules in ordinary chondrites. *Meteoritics & Planetary Science* 44:1561–1588.

Kearsley A. T., Burchell M. J., Price M. C., Graham G. A., Wozniakiewicz P. J., Cole M. J., Foster N. J., and Teslich N. 2009. Interpretation of Wild 2 dust fine structure: Comparison of Stardust aluminum foil craters to the three-dimensional shape of experimental impacts by artificial aggregate particles and meteorite powders. *Meteoritics & Planetary Science* 44:1489–1509.

Keller L. and Messenger S. 2007. Coordinated chemical and isotopic studies of IDPs: comparison of circumstellar and solar GEMS grains. 70th Annual Meteoritical Society Meeting, held in August 13–17, 2007, Tucson, Arizona. *Meteoritics & Planetary Science* 42:5297.

Kellerhals R., Shaw J., and Arora V. K. 1975. On grain size from thin sections. *Journal of Geology* 83:79–96.

Leroux H., Doukhan J.-C., and Guyot F. 2000. Metal-silicate interaction in quenched shock-induced melt of the Tenham L6-chondrite. *Earth and Planetary Science Letters* 179:477–487.

Leroux H., Rietmeijer F. J. M., Velbe M. A., Brearley A. J., Jacob D., Langenhorst F., Bridges J. C., Zega T. J., Stroud R. M., Cordier P., Harvey R. P., Lee M., Gounelle M., and Zolensky M. E. 2008a. A TEM study of thermally modified Comet 81P/Wild 2 dust particles by interactions with the aerogel matrix during the Stardust capture process. *Meteoritics & Planetary Science* 43:97–120.

Leroux H., Jacob D., Stodolna J., Nakamura-Messenger K., and Zolensky M. E. 2008b. Igneous Ca-rich pyroxene in comet 81P/Wild 2. *American Mineralogist* 93:1933–1936.

Leroux H., Roskosz M., and Jacob D. 2009. Oxidation state of iron and extensive redistribution of sulfur in thermally modified Stardust particles. *Geochimica et Cosmochimica Acta* 73:767–777.

Mantzaris N. V. 2005. Liquid-phase synthesis of nanoparticles: Particle size distribution dynamics and control. *Chemical Engineering Science* 60:4749–4770.

Nakamura T., Tsuchiyama A., Akaki T., Uesugi K., Nakano T., Takeuchi A., Suzuki Y., and Noguch T. 2008. Bulk mineralogy and three-dimensional structures of individual Stardust particles deduced from synchrotron X-ray diffraction and microtomography analysis. *Meteoritics & Planetary Science* 43:247–259.

Nguyen A. N., Stadermann F. J., Zinner E., Stroud R. M., Alexander C. M. O'D., and Nittler L. R. 2007. Characterization of presolar silicate and oxide grains in primitive carbonaceous chondrites. *Astrophysical Journal* 656:1223–1240.

Noguchi T., Nakamura T., Okudaira K., Yano H., Sugita S., and Burchell M. J. 2007. Thermal alteration of hydrated minerals during hypervelocity capture to silica aerogel at the flyby speed of Stardust. *Meteoritics & Planetary Science* 42:357–372.

Ratke L. 1988. Immiscible alloys under microgravity conditions. *Advances in Space Research* 8:7–16.

Ratke L. 1995a. Coarsening of liquid Al-Pb dispersions under microgravity – a EURECA experiment. *Advances in Space Research* 16:95–99.

Ratke L. 1995b. Coarsening of liquid Al-Pb dispersions under reduced gravity conditions. *Materials Science and Engineering* 203:399–407.

Ratke L. and Diefenbach S. 1995. Liquid immiscible alloys. *Materials Science and Engineering* 15:263–347.

Rietmeijer F. J. M. 2009a. Chemical identification of comet 81P/Wild 2 dust after interacting with molten aerogel. *Meteoritics & Planetary Science* 44:1121–1132.

Rietmeijer F. J. M. 2009b. A cometary aggregate interplanetary dust particle as an analog for comet Wild 2 grain chemistry preserved in silica-rich Stardust glass. *Meteoritics & Planetary Science* 44:1589–1609.

Rietmeijer F. J. M. 2009c. Stardust glass: Indigenous and modified comet Wild 2 particles. *Meteoritics & Planetary Science* 44:1707–1715.

Rietmeijer F. J. M., Nakamura T., Tsuchiyama A., Uesugi K., Nakano T., and Leroux H. 2008. Origin and formation of iron silicide phases in the aerogel of the Stardust mission. *Meteoritics & Planetary Science* 43:121–134.

Roskosz M., Leroux H., and Watson H. C. 2008. Thermal history, partial preservation and sampling bias recorded by Stardust cometary grains during their capture. *Earth and Planetary Science Letters* 273:195–202.

Sechremeli D., Stampouli A., and Stamtoudis M. 2006. Comparison of mean drop sizes and drop size distributions in agitated liquid-liquid dispersions produced by disk and open type impellers. *Chemical Engineering Journal* 117:117–122.

Sekigawa C. and Keller L. P. 2010. The mineralogy, petrography and chemistry of comet dust: Sulfides. (abstract #2405). 41st Lunar and Planetary Science Conference. CD-ROM.

Siegal R. W. 1991. Cluster-assembled nanophase materials. *Annual Review of Materials Science* 21:559–578.

Stephan T., Flynn G. J., Sandford S. A., and Zolensky M. E. 2008. TOF-SIMS analysis of cometary particles extracted from Stardust aerogel. *Meteoritics & Planetary Science* 43:285–298.

Stodolna J., Jacob D., and Leroux H. 2009. A TEM study of four particles extracted from the Stardust track 80. *Meteoritics & Planetary Science* 44:1511–1518.

Stone H. A. 1994. Dynamics of drop deformation and breakup in viscous fluids. *Annual Review of Fluid Mechanics* 26:65–102.

Tody D. 1993. IRAF in the Nineties. *A.S.P. Conference Series* 52:173.

Tomeoka K., Tomioka N., and Ohnishi I. 2008. Silicate minerals and SiO glass in comet Wild 2 samples: Transmission electron microscopy. *Meteoritics & Planetary Science* 43:273–284.

Trigo-Rodríguez J. M., Domínguez G., Burchell M. J., Hörz F., and Llorca J. 2008. Bulbous tracks arising from

hypervelocity capture in aerogel. *Meteoritics & Planetary Science* 43:75–86.

Tsuchiyama A., Nakamura T., Okazaki T., Uesugi K., Nakano T., Sakamoto K., Akaki T., Iida Y., Kadano T., Jogo K., and Suzuki Y. 2009. Three-dimensional structures and elemental distributions of Stardust impact tracks using synchrotron microtomography and X-ray fluorescence analysis. *Meteoritics & Planetary Science* 44:1203–1224.

Velbel M. A. and Harvey R. P. 2009. Along-track compositional and textural variation in extensively melted grains returned from comet 81P/Wild 2 by the Stardust mission: Implications for capture-melting process. *Meteoritics & Planetary Science* 44:1519–1540.

Villermaux E. 2007. Fragmentation. *Annual Reviews of Fluid Mechanics* 39:419–446.

Wang T. G., Trinh E. H., Croonquist A. P., and Elleman D. D. 1990. Dynamics of rotating and oscillating free drops. *American Institute of Physics Conference Proceedings* 197:106–111.

Wang T. G., Anilkumar A. V., Lee C. P., and Lin K. C. 1994. Bifurcation of rotating liquid drops: Results from USML-1 experiments in space. *Journal of Fluid Mechanics* 276:389–403.

Wozniakiewicz P. J., Kearsley A. T., Burchell M. J., Foster N. J., Cole M. J., Bland P.A., and Russell S. S. 2009. In situ analysis of residues resulting from laboratory impacts into aluminum 1100 foil: Implications for Stardust crater analysis. *Meteoritics & Planetary Science* 44:1541–1559.

Zolensky M. E., Zega T. J., Yano H., Wirick S., Westphal A. J., Weisberg M. K., Weber I., Warren J. L., Velbel M. A., Tsuchiyama A., Tsou P., Toppani A., Tomioka N., Tomeoka K., Teslich N., Taheri M., Susini J., Stroud R., Stephan T., Stadermann F. J., Snead C. J., Simon S. B., Simionovici A., See T. H., Robert F., Rietmeijer F. J. M., Rao W., Perronnet M. C., Papanastassiou D. A., Okudaira K., Ohsumi K., Ohnishi I., Nakamura-Messenger K., Nakamura T., Mostefaui S., Mikouchi T., Meibom A., Matrajt G., Marcus M. A., Leroux H., Lemelle L., Le L., Lanzirotti A., Langenhorst F., Krot A., Keller L. P., Kearsley A., Joswiak D., Jacob D., Ishii H., Harvey R., Hagiya K., Grossman L., Grossman J. N., Graham G. A., Gounelle M., Gillet P., Genge M. J., Flynn G. J., Ferroir T., Fallon S., Ebel D. S., Dai Z. R., Cordier P., Chi M., Butterworth A. L., Brownlee D. E., Browning N., Bridges J. C., Brennan S., Brearley A., Bradley J. P., Bland P., and Bastien R. 2006. Mineralogy and petrology of Comet 81P/Wild 2 nucleus samples. *Science* 314:1735–1739.

Zolensky M., Nakamura-Messenger K., Fletcher L., and See T. 2008a. Curation, spacecraft recovery, and preliminary examination for the Stardust mission: A perspective from the curatorial facility. *Meteoritics & Planetary Science* 43:5–21.

Zolensky M., Nakamura-Messenger K., Rietmeijer F., Leroux H., Mikouchi T., Ohsumi K., Simon S., Grossman L., Stephan T., Weisberg M., Velbel M., Zega T., Stroud R., Tomeoka K., Ohnishi I., Tomioka N., Nakamura T., Matrajt G., Joswiak D., Brownlee D., Langenhorst F., Krot A., Kearsley A., Ishii H., Graham G., Dai Z. R., Chi M., Bradley J., Hagiya K., Gounelle M., and Bridges J. 2008b. Comparison of Wild-2 particles to chondrites and IDPs. *Meteoritics & Planetary Science* 43:261–272.

APPENDIX A

We present a new methodology for measuring the droplet size distribution of Fe-Ni-S inclusions in TEM images Stardust cometary grains. We have applied astronomical image analysis tools to measure the sizes of the nanoscale droplets in an objective and repeatable manner. We have optimized SExtractor for the segmentation of Stardust droplets on TEM images and characterized the completeness function of our detection procedure to correct for the sensitivity of the methodology as function of droplet size that could bias the shape of the distribution.

SExtractor 2.4.4 was implemented for object detection (Bertin and Arnouts 1996). SExtractor implements the following features to address the difficulties in image segmentation that we outlined in the Methods section.

- Background: A grid of local background averages is determined by iteratively sigma-clipping (removing outliers a given number of standard deviations from the median) the histogram of pixels within a square mesh of width specified by the BACK_SIZE parameter. The magnitude of the change in sigma during each iteration is used to identify crowded fields. A median filter over a number of background meshes specified by the BACK_FILTERSIZE parameter is then applied to the background grid. By the adjustment of these two parameters, many features produced by vesiculation, compression, and chattering can be removed before object identification is attempted. The resulting background map is then subtracted from the TEM image. An example background map produced with our optimized SExtractor configuration is given in Fig. 1.

- Threshold: SExtractor uses a detection threshold that is a multiple (specified by the DETECT_THRESH parameter) of the standard deviation of the local background. This acts as a simple mechanism for avoiding false-positive detections in crowded regions while allowing for high sensitivity where the background is smooth yet contrast is low (for example, dense, Mg-rich areas of the matrix).

- Crowding: The difficulty in segmenting overlapping objects is significant because the droplets tend to be congregated in vesicular regions of the sample. This issue can be exacerbated by background filtering, which tends to smooth out object edges. SExtractor implements multi-threshold deblending to distinguish overlapping objects. Essentially, local maxima are identified within objects and considered to be distinct detections if the integrated intensity of the secondary peak is greater than some fraction, user-defined by the DEBLEND_MINCONT parameter, of the

primary peak intensity. This process is repeated for up to 32 such "branches" in the default configuration. This methodology is optimized for segmenting astronomical sources and may not be ideal for droplets in TEM images, whose radial density distribution profile is generally much flatter than the brightness profile of astronomical sources. SExtractor deblending requires a minimum to exist between the objects' centers (a saddle) and therefore would not distinguish between objects with, for example, a top hat profile. The assumption of a particular profile also appears when assigning each pixel to one object or another in the deblended segmentations, which is done by assuming a Gaussian probability distribution around each local maximum.

- Shape: SExtractor segments images by attributing all contiguous pixels over the defined threshold to a particular object. The isophotal area of the object in square pixels is then output as the ISOAREA_IMAGE parameter. To construct the size distribution, we can assign a single-parameter size measurement to each object as if this area corresponds to a circle. Additionally, SExtractor fits an ellipse to every object measured and outputs the fit's ELLIPTICITY parameter.

- Size: While very small droplets still exacerbate detection, SExtractor provides an algorithmic (reproducible) system for segmenting these features in TEM images.

We optimize SExtractor for segmentation of Stardust TEM images and characterize its performance by empirically tuning the detection parameters described above through completeness simulations. We define completeness as the probability that our segmentation methodology will detect a droplet as a function of its size. To determine the completeness of a given set of detection parameters, we add several model droplets to an existing TEM image and run SExtractor on the composite image to see how many were detected. We perform completeness testing for a range of object radii from 1 to 8 pixels ($\sim$3 to 22 nm) in radius. The most valuable product of this completeness testing is a function that we can use to correct the measured size distribution for the sensitivity of our detection methodology as a function of droplet size.

In detail, the completeness simulations to optimize the SExtractor configuration consisted of the following steps performed on a particular TEM image. For the purposes of completeness testing, we used an image selected at random from the 20 in our sample: region #1 of grain #42.

- Characterize the noise properties of the TEM CCD imager. In particular, to evaluate the uniformity of the background, we must estimate the readnoise of the CCD: the noise floor introduced by the readout process of the chip. We estimate the gain and readnoise using a dark region of the image as a proxy for an unexposed ("bias") frame and a bright region as a proxy for a uniform ("flat") frame. We adopt values of 0.169 e$^-$/ADU (electrons per analog-digital units) for the gain and 1.528 e$^-$ for the readnoise.

- Model the droplet density profiles. Modeling was performed using the psf task in the IRAF package daophot to fit intensity distribution profiles to a random subset of 15 "typical" droplets from a real TEM image. The model then represents the average density distribution of that random subset and can be scaled to different radii. A list of 174 typical droplets of various sizes was selected by hand. For each of five different radii, a different random subset was chosen from this list to create three different model profiles.

- Add artificial droplets to the image. Twenty artificial droplets are added to each trial image. If many more droplets were added per trial, then they may become unrealistically crowded on the image. The droplets are added using the addstar task in the IRAF daophot package. To randomize the artificial droplets used in each trial, this task superimposes Poisson noise on the droplet density model according to the detector gain. The integrated surface density ("brightness") and placement coordinates are also randomized for each artificial droplet. Because these parameters are totally random and not weighted in any way, we note that the completeness simulations will not reflect the actual density and spatial distribution of the droplets. As a possible consequence, the simulations may, for example, overstate the total completeness of the segmentation process if the artificial droplets are too often placed in crowded fields of the image or because they are too often made less dense (lower contrast) than real droplets. However, the completeness distribution as a function of radius, and therefore the resulting size distribution, should not be very sensitive to this issue.

- Vary SExtractor parameters and apply them to the images. To test different SExtractor configurations, a parameter of interest is varied while all other SExtractor detection parameters are held constant. Each detection configuration is used to segment the trial image and output a "catalog" of detections of both the real and artificial droplets in the image.

- Match the SExtractor catalogs to the input catalog to determine completeness. The percentage of the artificial droplets which were detected is referred to as the "completeness rate." To make an estimate of the rate at which false positives are produced, the

SExtractor catalog is also compared to a list of 160 coordinates found by eye to be devoid of real droplets. The percentage of these 160 positions for which detections are reported is called the "false positive rate." The "total completeness" is then the completeness rate minus the false positive rate.

The optimal SExtractor parameters determined in this way and the program's default values are listed in Table A1. To demonstrate the effectiveness of the optimized SExtractor configuration, we present an SExtractor "segmentation image" in Fig. 2, which color codes each object detected, next to the original TEM image.

Once the optimal SExtractor configuration was determined, the full completeness distribution was determined by additional simulations on the same TEM image. In these simulations, the optimal SExtractor configuration is used (and is not varied) and the resolution is increased: model droplets are scaled to radial increments of 1px and about 17 times as many iterations of the simulation are performed as in the optimization testing. The result is the final completeness distribution reproduced in Fig. 3. The completeness for objects 1 px in radius (5.5 nm in diameter) and greater than 8 px in radius (44 nm in diameter) is negligible. The greatest completeness ($\sim$40%) is achieved at a radius of 4 px (22 nm in diameter). The fact that the majority of droplets of any size cannot be detected is certainly a consequence of the factors complicating image analysis enumerated in the previous section. Critically, the measured completeness as a function of radius allows us to correct for this deficiency so that it does not bias our results. The completeness distribution was fit by a polynomial, given in Fig. 3, and used to correct the measured droplet size distribution for detection efficiency as a function of radius.

The largest Fe-Ni-S inclusions (with diameter much greater than about 40 nm or 7 pixels), typified by the core-mantle structure, are not investigated here. Our detection method is insensitive to these droplets because they are so large as to be picked up by the background filter. Moreover, because these inclusions are an order of magnitude less abundant than the smaller, spherical "droplets," we are not able to accumulate a sufficient sample to investigate their size distribution from our 20 image dataset covering less than 50 μm^2. We note that their core-mantle structure presents issues for automated object detection, as the core itself or isolated components of the rim may be erroneously detected as smaller, individual droplets.

We derive an additional correction function to account for projection effects. Because the thickness of the ultramicrotome section (70–140 nm) is of order the same size as the largest droplets we measure, it is important to consider projection effects. Assuming spherical symmetry, a droplet with radius r whose center falls outside the edge of the section by a distance x will have an apparent cross-sectional radius $r_c = r\sqrt{1 - (x/r)^2}$.

To evaluate the consequences of this effect, we perform simulations where we assume an input size distribution and model the fractional discrepancy with the "measured" size distribution as a function of droplet diameter. We assume that the position of the droplets that appear in the image has a uniform probability to be anywhere within the section or as far as $2r$ outside the edge of the section. Motivated by the characteristics of the uncorrected size distribution described in the text, we take as an input size distribution a lognormal function with mean diameter = 2.5 nm and σ = 0.5 nm, which has a mode at $\sim$10 nm. However, the simulation is not very sensitive to these input parameters; if we vary the mean or σ by 25%, the derived correction factor for 15 nm droplets varies by $\leq$5%. With the assumption of random placement within the depth of the section, and taking, for example, the thinnest section in our allocations (70 nm thick), only 7% of the smallest droplets (5 nm diameter) and 41% of the largest droplets (50 nm diameter) have their measured radius reduced by projection. Only 1% of the smallest droplets and 5% of the largest droplets are severely affected ($r_c \leq 0.5r$).

Using these simulations, we derive a correction function for each section thickness that scales the number of grains detected of a given size up or down to match the input distribution (Fig. 3). For the 70 nm-thick section, this correction function has the effect of revising the number of 5 nm droplets downward by 10% and revising the number of 40 nm droplets upward by 21%. For the 140 nm section, the effect is only 6% and 12%, respectively. Counts for droplets $\sim$10 nm in size are affected by $\leq$2% for all sections. The projection correction is therefore much smaller than the completeness correction, which is smallest at $\sim$22 nm (increasing the counts by a factor of 2.6), and increases rapidly below $\sim$10 nm and above $\sim$30 nm. We note that a similar, analytic correction function was derived by Eisenhour (1996) for the case of CO chondrites, where the typical chondrule size was larger than the thin section thickness.

N. E. Sanders and M. A. Velbel

Table A1. Optimal SExtractor configuration determined by completeness testing.

SExtractor detection parameter	Function	Default value	Optimal value
DETECT_THRESH	Threshold for object detection in units of the background standard deviation.	1.500	2.675
BACK_SIZE	Size of regions averaged to produce background values, in pixels.	64.0	6.5
BACK_FILTERSIZE	Size of median filter applied to smooth the background, in pixels.	3	5
DEBLEND_MINCONT	Contrast ratio required for distinguishing overlapping objects.	0.005	0.010